


Helical superconducting edge modes from pseudo-Landau levels in graphene

Daniel Sabsovich¹, Marc W. Bockrath², Kirill Shtengel³, and Eran Sela¹

¹*Raymond and Beverly Sackler School of Physics and Astronomy, Tel Aviv University, Tel Aviv 69978, Israel*

²*Department of Physics, The Ohio State University, Columbus, Ohio 43210, USA*

³*Department of Physics and Astronomy, University of California at Riverside, Riverside, California 92521, USA*

 (Received 23 November 2020; revised 3 February 2021; accepted 11 March 2021; published 23 March 2021)

We explore Andreev states at the interface of graphene and a superconductor for a uniform pseudomagnetic field. Near the zeroth-pseudo-Landau level, we find a topological transition as a function of applied Zeeman field, at which a gapless helical mode appears. This one-dimensional mode is protected from backscattering as long as intervalley and spin-flip scattering are suppressed. We discuss a possible experimental platform to detect this gapless mode based on strained suspended membranes on a superconductor, in which dynamical strain causes charge pumping.

DOI: [10.1103/PhysRevB.103.094513](https://doi.org/10.1103/PhysRevB.103.094513)

I. INTRODUCTION

Synthetic gauge fields resulting from strain [1–5] have been observed in numerous experiments on graphene samples [6–9]. These gauge fields result from the movement of the Dirac points in momentum space, which results from the modification of the hopping amplitudes by strain [10,11]. This phenomenon is general for Dirac materials [12–17] and results in time-reversal symmetric pseudo-Landau levels (PLLs). In various geometries of graphene membranes, it is possible to engineer strain to yield uniform pseudomagnetic fields [10,18–20].

Since pseudomagnetic fields act oppositely on the two valleys of graphene, they may have a distinct interplay with superconductivity [21–30]. A usual superconducting order parameter involving pairing of time-reversal partners is blind to such a field. Nevertheless, the microscopic theory, critical temperature, and quasiparticle excitations are strongly affected by a pseudomagnetic field.

In this paper, we explore one-dimensional (1D) Andreev modes that can be stabilized on the interface between strained graphene and a superconductor [31,32]; see Fig. 1(a). In the presence of a real magnetic field, Akhmerov and Beenakker [33] found cyclotron orbits of Andreev reflected electrons and holes that are fully localized when the chemical potential lies at the Dirac point; see Fig. 1(b). Physically, a specular-reflected hole [32] proceeds along the mirror-reflected segment of the electronic cyclotron trajectory. In the case of a pseudomagnetic field, Gunawardana and Uchoa [34] found propagating states instead; see Fig. 1(c). By performing a mirror transformation to the hole trajectories and recalling that the pseudomagnetic field has opposite signs for the two valleys, those solutions become snake states, propagating on interfaces at which a magnetic field changes sign.

Here we study the interplay of the pseudomagnetic field B and a Zeeman magnetic field B_Z on the graphene-superconductor interface; see Fig. 1(a). We show that as B_Z

exceeds the chemical potential μ measured from the Dirac point, the 1D interface becomes gapless, hosting a helical 1D mode; see Fig. 1(d). Helical modes consist of counter-propagating Dirac fermions carrying opposite spin, similar to those realized on the edge of a 2D topological insulator [35] or in the zeroth Landau level in graphene subjected to a Zeeman field [36,37]. On the interface between a superconductor and a strained graphene, the helical modes appearing due to the Zeeman field are gapless Andreev states protected from backscattering as long as (i) the disorder is smooth and does not result in intervalley scattering, and (ii) spin flip is not possible. By contrast, in the case of a real magnetic field, superconducting pairing leads to the gapping of the helical edge modes, providing a platform for hosting Majorana zero modes at the boundaries of superconducting domains [38].

The paper is organized as follows. In Sec. II we solve the BdG equations describing graphene within the Dirac theory in the presence of a pairing potential step and pseudomagnetic field. We explore in detail the low-energy part undergoing a phase transition in Sec. III by projecting down to the zeroth PLL and treating superconductivity, the Zeeman field, and also spin-orbit coupling as perturbations. In Sec. IV we discuss a Thouless pumping experiment, taking place as the flux associated with the pseudomagnetic field varies in time. We conclude in Sec. V.

II. INTERFACE MODES

We consider a graphene sheet subjected to a uniform pseudomagnetic field B , proximitized by a superconductor covering the $x < 0$ region; see Fig. 1(d). We write the Bogoliubov–de Gennes (BdG) equation as

$$\begin{bmatrix} H - \mu & \Delta(x) \\ \Delta(x)^* & \mu - THT^{-1} \end{bmatrix} \Psi = \varepsilon \Psi, \quad (1)$$

where $\Delta(x) = \Delta$ for $x < 0$ and $\Delta(x) = 0$ for $x > 0$. T here is the time-reversal operator and μ is the chemical potential.

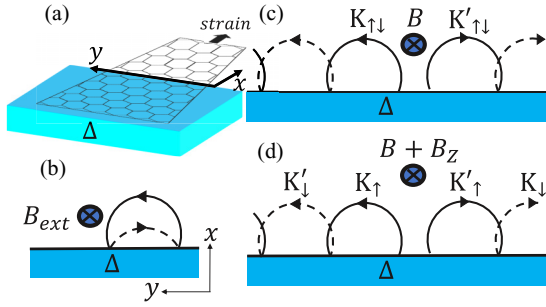


FIG. 1. (a) Schematics of a graphene ribbon deposited on a superconductor (Δ) for $x < 0$ and strained along x . The ($x = 0$) interface along y is assumed to be infinite. (b) Andreev interface modes for graphene near the neutrality point, for a real magnetic field B_{ext} [33], or (c) for a pseudomagnetic field B [34]. (d) With an additional Zeeman field B_Z , an Andreev helical mode is stabilized.

The 8×8 Hamiltonian H is decomposed as $H = H_0 + H_Z$, where H_0 describes the graphene and H_Z is a Zeeman term. Each piece can be written in terms of Pauli matrices τ , σ , and s acting in valley, pseudospin, and spin spaces, respectively. In the valley-symmetric notation [33], graphene in a pseudomagnetic field is described by the Hamiltonian

$$H_0 = v_F \sum_{i=x,y} (p_i \tau_0 \otimes \sigma_i + A_i \tau_z \otimes \sigma_i) \otimes s_0, \quad (2)$$

where v_F is the Fermi velocity. Written explicitly in the valley space, it reads

$$H_0 = v_F \begin{pmatrix} (\mathbf{p} + \mathbf{A}) \cdot \sigma & 0 \\ 0 & (\mathbf{p} - \mathbf{A}) \cdot \sigma \end{pmatrix} \otimes s_0. \quad (3)$$

Even in the presence of the pseudomagnetic field, H_0 is time-reversal symmetric, $H_0 = T H_0 T^{-1}$. Here $T = -i \tau_y \sigma_y s_y C$, where C denotes complex conjugation, satisfying $T^2 = -1$. On the other hand, $H_Z = B_Z \tau_0 \otimes \sigma_0 \otimes s_z$ describes a Zeeman field, which is time reversal odd, $H_Z = -T H_Z T^{-1}$.

In what follows, we use the Landau gauge $\mathbf{A} = Bx\hat{y}$. An eigenvector of the Hamiltonian in Eq. (3) in the K valley can be written as $\phi_K e^{ip_y y}$, where $\phi_K(x)$ is a 2-spinor satisfying

$$[(-i\partial_x)\sigma_x + (p_y + x)\sigma_y]\phi_K = \varepsilon\phi_K. \quad (4)$$

We measure length in units of magnetic length $\ell_B = \sqrt{\hbar/eB}$, momentum p_y in units of \hbar/ℓ_B , and energy in units of $\hbar v_F/\ell_B$. The 2-spinor solutions are

$$\begin{aligned} \Phi_K^{(n)} &= e^{-\frac{1}{2}\xi_+^2} \begin{pmatrix} -i\sqrt{2n}H_{n-1}(\xi_+) \\ \pm H_n(\xi_+) \end{pmatrix}_{\varepsilon=\pm\sqrt{2n}}, \\ \Phi_{K'}^{(n)} &= e^{-\frac{1}{2}\xi_-^2} \begin{pmatrix} \pm H_n(\xi_-) \\ -i\sqrt{2n}H_{n-1}(\xi_-) \end{pmatrix}_{\varepsilon=\pm\sqrt{2n}}, \end{aligned} \quad (5)$$

where $\xi_{\pm} = x \pm p_y$ and $H_n(x)$ are Hermite polynomials. As detailed in Appendix A, we proceed by using these solutions for the normal region $x > 0$ and imposing a boundary condition describing Andreev reflection [33,39], which is valid when the superconducting coherence length is smaller than ℓ_B .

The dispersion relation $\varepsilon(p_y)$ is plotted in Fig. 2. The momentum along the interface, p_y , determines the position

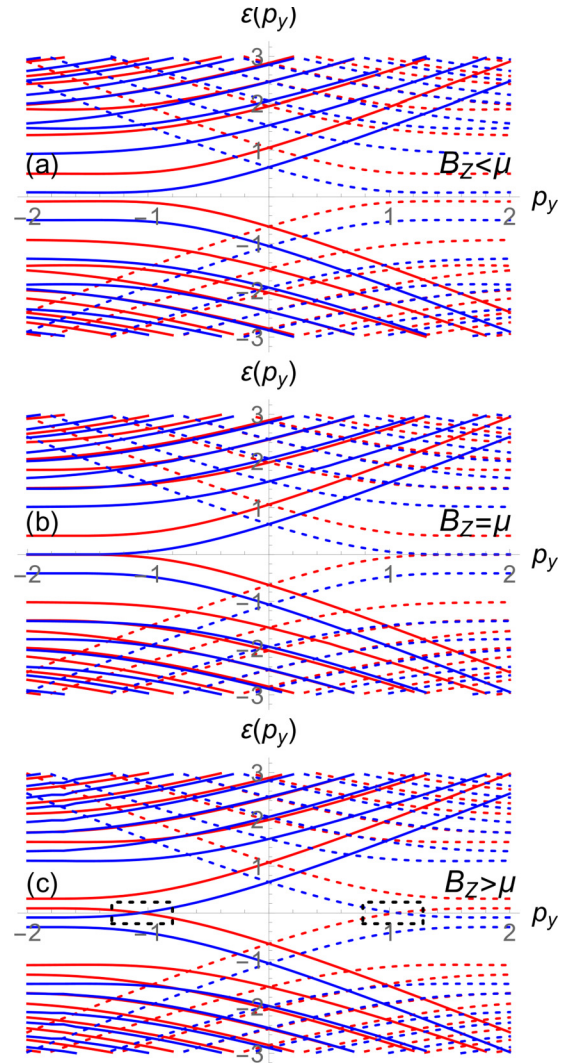


FIG. 2. Dispersion relation $\varepsilon(p_y)$ of Andreev states at a 1D interface between proximitized graphene and normal graphene with PLLs, obtained by solving Eq. (A10) for $\Delta = 10$, $B_Z = 0.2$. We use red/blue to describe opposite spins, and full/dashed lines to describe opposite valleys. Panel (a) shows a gapped spectrum at $\mu = 0.3$; (b) the gap closes at $\mu = 0.2$; (c) gapless helical interface modes are marked by dashed rectangles for $\mu = 0.1$.

along the x -axis; for K (K') the electron wave function is localized near $x = -p_y$ ($x = p_y$). Solid lines represent valley- K electron states, which for negative momentum approach the $\pm\sqrt{2n}$ values of the PLLs for $B_Z = \mu = 0$ (not shown), and correspond to states localized in the normal region. For increasing p_y , the modes acquire a dispersion due to the pairing potential $\Delta(x)$ inside the superconducting region. The opposite p_y - x relation applies for K' states (dashed lines).

This model has two phases in the μ - B_Z plane. For $|\mu| < |B_Z|$, we have gapless 1D interface modes, as seen in Fig. 2(c). By contrast, for $|\mu| > |B_Z|$, the interface is gapped, as seen in Fig. 2(a). At the transition $|\mu| = |B_Z|$ [see Fig. 2(b)], the PLL excitation gap closes at the normal side. The corresponding phase diagram is shown in Fig. 3 for the regime where μ and B_Z are small compared to the PLL separation $\hbar v_F/\ell_B$.

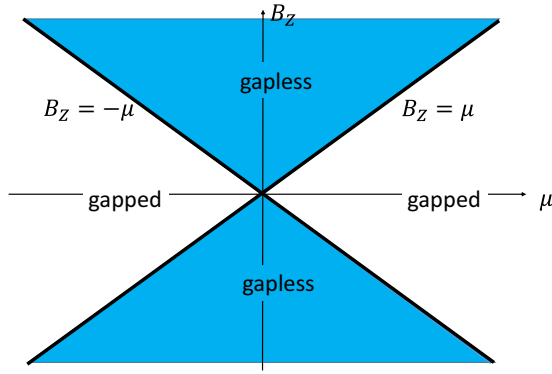


FIG. 3. Phase diagram of our superconductor-normal (SN) interface for B_z, μ smaller than the PLL spacing.

In Appendix B we demonstrate the emergence of gapless 1D interface modes using a tight-binding model, reproducing the same low-energy physics even when additional lattice effects are present, such as zigzag edge states. In Appendix A we discuss what happens when the Zeeman field B_z exceeds the PLL gap. Below we focus on the low-energy part by restricting the theory to the zeroth PLL.

III. PROJECTION TO THE ZEROTH PLL

We proceed by projecting the Hamiltonian to the zeroth PLL. This approach is valid for $B_z, \mu, \Delta \ll \hbar v_F / \ell_B$. The normalized zero-energy solutions of H_0 in Eq. (5) are

$$\Phi_K^{(n=0)} = \frac{1}{\pi^{1/4}} e^{-\frac{1}{2}\xi_+^2} \begin{pmatrix} 0 \\ 1 \end{pmatrix}, \quad \Phi_{K'}^{(n=0)} = \frac{1}{\pi^{1/4}} e^{-\frac{1}{2}\xi_-^2} \begin{pmatrix} 1 \\ 0 \end{pmatrix}. \quad (6)$$

We use the valley-symmetric notation in which the two sublattices are interchanged for valley K' . For a given p_y the dimension of the degenerate zero-energy space of the BdG matrix Eq. (1) is 8, which includes an additional duplication due to particles and holes. We introduce a basis $|\tau^z, s^z, \eta^z\rangle$ ($\tau^z, s^z, \eta^z = \pm$) denoting the valley, spin, and particle-hole spaces, respectively. Equivalently, in Eq. (1) we can use the Bogoliubov spinor

$$\Psi = (\psi_{K\uparrow}, \psi_{K\downarrow}, \psi_{K'\uparrow}, \psi_{K'\downarrow}, \psi_{K'\downarrow}^\dagger, -\psi_{K'\uparrow}^\dagger, \psi_{K\downarrow}^\dagger, -\psi_{K\uparrow}^\dagger) \quad (7)$$

whose eight components are defined in the basis $|\tau^z, s^z, \eta^z\rangle$ as

$$\begin{aligned} &|+++\rangle, |+-+\rangle, |-++\rangle, |--+\rangle, \\ &|+ +- \rangle, |+ -- \rangle, |- +- \rangle, |- - - \rangle \equiv |1\rangle, \dots, |8\rangle. \end{aligned} \quad (8)$$

We now project the various terms of the BdG Hamiltonian in Eq. (1). Consider the pairing part of the Hamiltonian first:

$$\mathcal{H}_\Delta = \begin{pmatrix} 0 & \Delta(x) \\ \Delta^*(x) & 0 \end{pmatrix}.$$

It has matrix elements

$$\begin{aligned} \langle +s^z \mp | \mathcal{H}_\Delta | +s^z \pm \rangle &= \Delta \int_{-\infty}^0 \frac{1}{\sqrt{\pi}} e^{-(x+p_y)^2} dx \equiv \Delta F(p_y), \\ \langle -s^z \mp | \mathcal{H}_\Delta | -s^z \pm \rangle &= \Delta F(-p_y). \end{aligned} \quad (9)$$

The function $F(p_y)$, describing the matrix element of the pairing potential in a state with momentum p_y , behaves as

$F(p_y) \rightarrow 1$ for $p_y \rightarrow \infty$ and $F(p_y) \cong \frac{e^{-p_y^2}}{2\sqrt{\pi}|p_y|}$ for $p_y \rightarrow -\infty$. Physically, for positive p_y the support of wave functions in Eq. (6) corresponding to valley K is well within the superconductor, while for negative p_y it is mainly in the normal region. In the latter case, the wave functions are affected by the pairing potential only through their exponential tail. Hence,

$$\mathcal{H}_\Delta(p_y) = \frac{\Delta}{2} [F(p_y)(\tau_0 + \tau_z) + F(-p_y)(\tau_0 - \tau_z)] \otimes s_0 \otimes \eta_x. \quad (10)$$

Similarly, the Zeeman term takes the form

$$\mathcal{H}_Z(p_y) = B_z \tau_0 \otimes s_z \otimes \eta_0. \quad (11)$$

The eigenvalues of the projected zeroth-PLL Hamiltonian,

$$\mathcal{H}_{0LL}(p_y) = \mathcal{H}_Z(p_y) + \mathcal{H}_\Delta(p_y) - \mu \eta_z, \quad (12)$$

are plotted in Fig. 4 for various values of B_z and μ , reproducing the low-energy sector seen in Fig. 2.

Let us focus on the four solutions at large negative p_y , which are basically unaffected by Δ . They originate from electrons in valley K or holes of valley K' (not dashed). Their energies are

$$\begin{aligned} \varepsilon_1(e_{K\uparrow}) &= B_z - \mu - \lambda_I, \\ \varepsilon_2(e_{K\downarrow}) &= -B_z - \mu + \lambda_I, \\ \varepsilon_5(h_{K'\downarrow}) &= B_z + \mu + \lambda_I, \\ \varepsilon_6(h_{K'\uparrow}) &= -B_z + \mu - \lambda_I. \end{aligned} \quad (13)$$

In Sec. III B we will introduce the spin-orbit coupling λ_I and discuss its role; for now we set $\lambda_I = 0$. Here the subscripts refer to components of the Bogoliubov spinor Ψ ; see Eqs. (7) and (8). We can see in Fig. 4 that Δ separately couples modes 1 and 5 ($K \uparrow$ and $K' \downarrow$) as marked by red curves, which diverge as p_y increases, and similarly 2 and 6 ($K \downarrow$ and $K' \uparrow$) shown as diverging blue curves. Let us denote the corresponding level separations by $\Delta_{1,2}$, respectively. As can be seen in Fig. 4(c), in the topological phase $|B_z| > \mu$ this level repulsion leads to zero-energy edge states.

Consider the left-moving gapless quasiparticles denoted γ_L originating from the $p_y < 0$ region due to the Δ_1 sector in Fig. 4(c). Along with the gapped partner denoted χ , this pair [red solid curves in Fig. 4(c)] can be expressed as a combination of $\psi_{K\uparrow, p}$ and $\psi_{K'\downarrow, -p}$ in the form

$$\begin{aligned} \text{gapless} : \gamma_{L, p_y} &= u_{p_y} \psi_{K\uparrow, p_y} + v_{p_y} \psi_{K'\downarrow, -p_y}^\dagger, \\ \text{gapped} : \chi_{p_y} &= -v_{p_y} \psi_{K\uparrow, p_y} + u_{p_y} \psi_{K'\downarrow, -p_y}^\dagger. \end{aligned} \quad (14)$$

Similarly, consider the red dashed pair of curves in Fig. 4(c) forming the Δ_2 sector. They lead to a right-moving gapless mode γ_R , and a gapped mode denoted χ' ,

$$\begin{aligned} \text{gapless} : \gamma_{R, p_y} &= u'_{p_y} \psi_{K'\uparrow, p_y} + v'_{p_y} \psi_{K\downarrow, -p_y}^\dagger, \\ \text{gapped} : \chi'_{p_y} &= -v'_{p_y} \psi_{K'\uparrow, p_y} + u'_{p_y} \psi_{K\downarrow, -p_y}^\dagger. \end{aligned} \quad (15)$$

These 1D modes are Dirac rather than Majorana fermions. Namely, $\gamma_L \neq \gamma_L^\dagger$ and $\gamma_R \neq \gamma_R^\dagger$. Considering, for example, γ_R in the $p_y > 0$ region (red-dashed), given in Eq. (15), and applying Hermitian conjugation, one obtains the right-moving

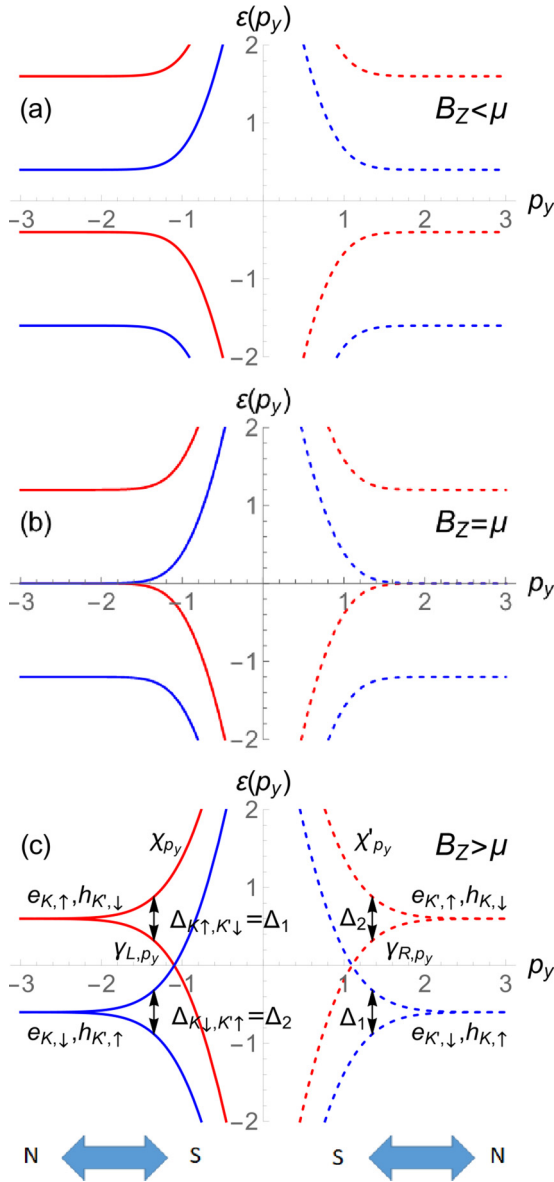


FIG. 4. Dispersion relation of our SN interface (as in Fig. 3) focusing on the zeroth PLL using Eq. (12), setting $\Delta = 10$ and $B_Z = 0.6$. In (a) $\mu = 1$ and we have a gapped interface. As we decrease μ , the gap decreases and eventually closes in (b) at $\mu = 0.6$. The condition $|\mu| < |B_Z|$ leads to a gapless helical Dirac fermion as seen in (c), where $\mu = 0$. At the bottom we illustrate the x - p_y relationship.

gapless mode in the $p_y < 0$ region (blue-solid). Thus we have both particle and hole excitations, formed out of the quasiparticle operators, allowing us to define Dirac fermions. Linearizing the spectrum near $\varepsilon = 0$, the low-energy Hamiltonian is

$$H_{\text{Dirac}} = v_0 \sum_{p_y} [(p_y - p_0)\gamma_{R,p_y}^\dagger \gamma_{R,p_y} - (p_y + p_0)\gamma_{L,p_y}^\dagger \gamma_{L,p_y}]. \quad (16)$$

It is valid for energies low compared to $\min\{\varepsilon_1, \varepsilon_2, \varepsilon_5, \varepsilon_6\}$; see Eq. (13).

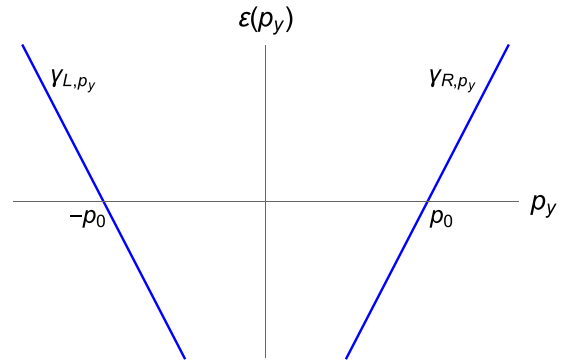


FIG. 5. Low-energy spectrum describing the helical Dirac mode. The right- and left-moving excitations are described in Eqs. (14) and (15), and the Dirac Hamiltonian is given in Eq. (16).

The resulting counterpropagating Dirac modes are similar to the edge states in the quantum-spin Hall effect. While we consider noninteracting electrons, interactions as well as disorder on the edge can be treated as is done in the context of the quantum spin Hall effect [40–42].

A. $\mathbb{Z}_2 \times \mathbb{Z}_2$ symmetry

Usually proximity-induced superconductivity $\sum_i \Delta c_{i\uparrow}^\dagger c_{i\downarrow}^\dagger$ breaks $U(1)$ charge conservation down to \mathbb{Z}_2 , the parity conservation:

$$P = e^{i\pi \sum_{j,\sigma} c_{j,\sigma}^\dagger c_{j,\sigma}}. \quad (17)$$

At energy sufficiently low compared to the bandwidth of graphene, the pairing Hamiltonian becomes $\int dr [\Delta_1 \psi_{K\uparrow}^\dagger \psi_{K'\downarrow}^\dagger + \Delta_2 \psi_{K'\uparrow}^\dagger \psi_{K\downarrow}^\dagger + \text{H.c.}]$, with the two terms accounting for the two valleys at opposite momenta. While $\Delta_1 = \Delta_2 = \Delta$, this form emphasizes that we have two conserved parities,

$$P_1 = e^{i\pi \int d^2r (\psi_{K\uparrow}^\dagger \psi_{K\uparrow} + \psi_{K'\downarrow}^\dagger \psi_{K'\downarrow})}, \quad (18)$$

$$P_2 = e^{i\pi \int d^2r (\psi_{K\downarrow}^\dagger \psi_{K\downarrow} + \psi_{K'\uparrow}^\dagger \psi_{K'\uparrow})}.$$

This $\mathbb{Z}_2 \times \mathbb{Z}_2$ parity symmetry applies as long as the following two processes are suppressed: intervalley scattering, $H_{i-v} = V_{iv} \sum_{\sigma,p_y} \psi_{K\sigma,p_y}^\dagger \psi_{K'\sigma,p_y} + \text{H.c.}$, and spin-flip scattering, $H_{s-f} = V_{sf} \sum_{p_y} \psi_{K\uparrow,p_y}^\dagger \psi_{K\downarrow,p_y} + \psi_{K'\uparrow,p_y}^\dagger \psi_{K'\downarrow,p_y} + \text{H.c.}$. Both processes break the separate conservation of P_1 and P_2 down to a single \mathbb{Z}_2 symmetry corresponding to the conservation of $P_1 P_2$. Expressed in terms of the low-energy quasiparticle excitations, H_{i-v} becomes $H_{i-v} \sim V_{iv} \sum_{p_y} \gamma_{L,p_y}^\dagger \gamma_{R,p_y} + \text{H.c.}$. A spatially uniform intervalley scattering term does not open a gap since generally scattering between the two Dirac modes requires momentum transfer; see Fig. 5. However, sufficiently short-range disorder can enable such momentum transfer, and hence backscattering. In the quasiparticle language, H_{s-f} becomes $H_{s-f} \sim V_{sf} \sum_{p_y} \gamma_{L,p_y}^\dagger \gamma_{R,-p_y} + \text{H.c.}$ Naively, one would expect that the level crossing at $\varepsilon = 0$ would become avoided for the Zeeman magnetic field tilted away from the z axis. However, this intuition is incorrect, and the gapless mode persists irrespective of the direction of the field as long as a $U(1)$ conservation of the spin along some direction persists. In that

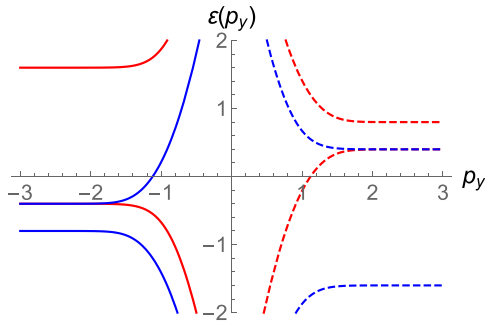


FIG. 6. Low-energy dispersion from Eq. (12) with the addition of SOC Eq. (20). Here $\Delta = 10$, $B_Z = \lambda_I = 0.6$, and $\mu = 0.4$.

case, one can redefine a corresponding conserved $\mathbb{Z}_2 \times \mathbb{Z}_2$. However, as discussed in the next subsection, in the presence of spin-orbit coupling, tilting the direction of the Zeeman field does open a gap due to the quasiparticle backscattering.

In general, zero-energy solutions to the BdG equation reflect a degeneracy between ground states with different parity. In our model, for $|B_Z| > |\mu|$ we have $\varepsilon \rightarrow 0$ quasiparticle solutions that change either P_1 (γ_L) or P_2 (γ_R), allowing us to identify four ground states.

It is interesting to note that the association of left-movers with $\Delta_1 = \Delta_{K\uparrow, K'\downarrow}$ and of right-movers with $\Delta_2 = \Delta_{K'\uparrow, K\downarrow}$ switches upon switching the sign of the Zeeman field.

B. Spin-orbit coupling

Intrinsic spin-orbit coupling (SOC) in graphene, which in the standard notation [43] takes the form $\lambda_I \tau_z \otimes \sigma_z \otimes s_z$, becomes in our valley-symmetric notation

$$H_{\text{SO}} = \lambda_I \tau_0 \otimes \sigma_z \otimes s_z. \quad (19)$$

Projecting this time-reversal symmetric term to the zeroth PLL subspace, its contribution to the BdG matrix Eq. (1), using Eq. (6), becomes

$$\mathcal{H}_{\text{SO}} = -\lambda_I \tau_z \otimes s_z \otimes \eta_z. \quad (20)$$

While the phase diagram in Fig. 3 reflects a phase transition occurring in both \mathbb{Z}_2 sectors, in the presence of SOC one can induce a phase transition separately in each sector. One can generalize the arguments about the level repulsion due to Δ_1 or Δ_2 for the presence of SOC. In this case, the energies of the four states in the normal region are given in Eq. (13) with λ_I included. The condition for the topological phase in the Δ_1 sector (Δ_2 sector) is that ε_1 and ε_5 (ε_2 and ε_6) have opposite signs. One can achieve these conditions independently. An example is shown in Fig. 6, where only the Δ_2 sector is topological, with two right-moving branches, composing one right-moving chiral Dirac fermion, and no left-movers. This exemplifies a quantum Hall state stabilized by a Zeeman field and SOC. In this case, the edge states are chiral and hence protected against either spin-flip or intervalley scattering.

C. Other pairing channels

We remark that we have considered s -wave pairing in Eq. (1), but our model allows us to consider more general pairings. In our $\mathbb{Z}_2 \times \mathbb{Z}_2$ decomposition, s -wave pairing

is reflected in equal pairings in each \mathbb{Z}_2 sector, $\Delta_1 = \Delta_2$, where we recall that $\Delta_1 = \Delta_{K\uparrow, K'\downarrow}$ and $\Delta_2 = \Delta_{K'\uparrow, K\downarrow}$. However, one can consider any combination of singlet and triplet pairings, $\Delta_1 = \Delta_s + \Delta_t$, $\Delta_2 = \Delta_s - \Delta_t$. This provides an additional knob for tuning the topological transition in each \mathbb{Z}_2 sector. Here we remark that close to the extreme case of equal superposition of singlet and triplet pairing, implying $\Delta_2 = 0$ (or $\Delta_1 = 0$), similar to the case of strong spin-orbit coupling in Fig. 6, we can have a situation in which only the Δ_1 (or Δ_2) sector is topological.

D. Symmetry classification

Like any weakly interacting fermionic system, our model can be classified according to the Altland-Zirnbauer symmetry classes. The superconducting system considered here has neither time-reversal nor spin-rotation symmetry, hence it belongs to class D [44] (see also Table I in Ref. [45]). Since our system has conserved S^z , implying a superconductor with $\mathbb{Z}_2 \times \mathbb{Z}_2$ parity symmetry, its symmetry classification corresponds to two sectors, each of which is in class D .

Class D superconductors in two dimensions are characterized by a topological \mathbb{Z} index, counting the number of chiral Majorana fermions on the edge with vacuum. The 1D interface under consideration here, on the other hand, is an interface with a normal system (nonsuperconducting symmetry class A). Nevertheless, as we discuss in Appendix B 1, the interface with vacuum has indeed edge states when the Zeeman field exceeds the pairing gap. It is interesting that the two parity sectors generically can have unrelated \mathbb{Z} indices, whereas a helical-like state is characterized by two opposite indices. The occurrence of Dirac rather than Majorana fermions implies that in our system the \mathbb{Z} index is restricted even integers.

IV. PUMPING

Consider a circular geometry with the superconductor covering the region $r > R$. Imagine that the pseudomagnetic field is uniform in space and changes in time slowly. As we explain next, in this dynamical process charge is pumped into or out of the normal region, through the NS interface.

First consider the region $\Delta = 0$ at $r < R$. dB/dt generates an azimuthal pseudo-electric field $\vec{E} = -\frac{d\vec{A}}{dt}$; Together with the pseudomagnetic field, we have a drift velocity $\vec{v}_d = \frac{\vec{E} \times \vec{B}}{|\vec{B}|^2}$ along the radial direction; see Fig. 7(a). The drift velocity has the same sign for the two valleys [20]. The resulting charge current into a region of radius r is

$$\frac{dQ(r)}{dt} = \oint_r \vec{j}(r) \cdot d\vec{\ell} = 2\pi r n_e e \frac{E(r)}{B}, \quad (21)$$

where we used $j = n_e e v_d$ for the inward charge current density. Assuming that the density, n_e , is determined by the filling factor ν as $n_e = \frac{B}{\Phi_0} \nu$, we have

$$\frac{dQ(r)}{dt} = n_e e \frac{\pi r^2 \dot{B}}{B} = e \frac{\dot{\Phi}}{\Phi_0} \nu. \quad (22)$$

Thus the change in the number of particles coincides with ν times the change in the number of flux quanta of the pseudomagnetic field.

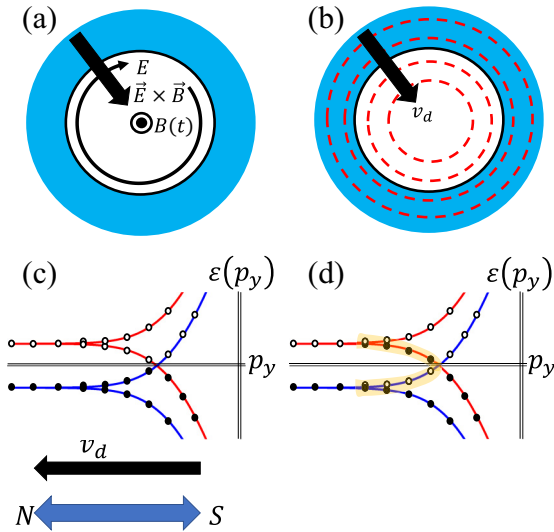


FIG. 7. Charge pumping: (a) Circular NS interface with a time-dependent pseudomagnetic field \hat{B} creating a pseudoelectric field E . The crossed E and B pseudofields result [20] in a radial charge current. (b) Ringlike PLL solutions adiabatically shrink as B increases. (c) Quantized momenta and their occupation in the instantaneous ground state. These bands correspond to the left side ($p_y < 0$) of Fig. 5(c). The black arrow denotes the drift in p_y as B increases. In the $p_y > 0$ region, the drift is in the opposite direction in momentum space, and in the same spatial direction, not shown. (d) Excited state resulting from pumping. Marked are excited single-quasiparticle states within the gapless helical branch.

Equivalently, consider the adiabatic evolution of the many-body wave function generated by \hat{B} . In the radial geometry, p_y corresponds to angular momentum and is quantized, together with the radius of the ring-orbitals, as

$$p_j = \frac{\hbar}{\ell_B} \sqrt{j}, \quad r_j = \ell_B \sqrt{j}, \quad j \in \mathbb{N}. \quad (23)$$

The values of p_j and r_j change upon increasing B in such a way that the r_j 's become denser; see Fig. 7(b). The particle density remains locked to the instantaneous value of B according to $n_e = \frac{B}{\phi_0} \nu$.

A. Pumping through the interface

Now we discuss the role of the SN interface $r \sim R$. Does the many-body state resulting from the motion in p_y -space coincide with the instantaneous ground state? The answer is positive if the BdG spectrum of the interface is gapped, as in the trivial phase $|\mu| > |B_Z|$. However, the answer is negative for $|B_Z| > |\mu|$. In this case, Fig. 7(c) represents schematically the occupation of BdG states near the left crossing in Fig. 4(c) before pumping. We can see that occupied states form only subsets of BdG bands. As the spectral flow occurs, from the superconductor to the normal region, the p_j 's move to the left. The resulting many-body state in Fig. 7(d) is an excited state.

Thus, the gapless bands at the interface influence pumping by creating excitations. While we do not treat this explicitly, relaxation will eventually occur and create dissipation. On the

other hand, no dissipation is expected in the gapped regime $|B_Z| < |\mu|$.

B. Possible experimental realization

Finally, we mention a possible realization of this system. On a practical level, our setup requires systems with controlled pseudomagnetic fields. Designs of graphene membranes with programmable strain in order to engineer nearly uniform pseudomagnetic fields over macroscopic distances have been proposed [10, 18–20]. One such platform consists of a graphene flake suspended on top of a triangular aperture, with the sides normal to the (100) crystallographic axes of the graphene membrane. In this system, a few-Tesla pseudofield can be generated over a micrometer scale by electrostatically pulling the membrane toward a gate [10]. This platform can then allow us to induce pairing correlations on PLLs using a superconducting substrate.

In the same system with the pseudomagnetic field controlled by a gate, one can pump electrons in and out of the membrane simply by oscillating the gate potential, while the nanomechanical quality factor and frequency of the membrane could in principle be detected using approaches such as those described in Ref. [46]. The charge pumping itself can be detected via a shift of the mechanical resonance frequency. An explicit treatment of pumping in such a device remains a subject a future study.

Another possible detection scheme is based on a rectification of the ac pumped current. One may create a current path from one side of the membrane to the other [47]. A rectified dc current could be created, e.g., using an additional ac control of the relative resistance between the membrane and the two contacts.

V. CONCLUSIONS

We studied a 1D interface between graphene with a strain-induced pseudomagnetic field and a superconductor. Adding a Zeeman magnetic field, we identified a phase that supports helical edge modes. They are protected by a $\mathbb{Z}_2 \times \mathbb{Z}_2$ symmetry, reflecting the separate conservation of either (K, \uparrow) and (K', \downarrow) electrons, or of (K', \uparrow) and (K, \downarrow) electrons. This emergent symmetry of proximitized graphene becomes exact when intervalley and spin-flip scatterings are suppressed. SOC allows to eliminate either the right-going or the left-going edge modes, resulting in a chiral edge mode.

Recently there have been numerous experiments exploring the interface of graphene with superconductors in the presence of real magnetic fields [48–55]. Supplementing this setting with controlled strain is an important future direction. We discussed a possible experimental realization of a pseudomagnetic field in a strained membrane that would allow one to probe the predicted edge states. We demonstrated that in our time-reversal symmetric PLLs, ac modulation of the pseudofield results in charge pumping. This charge pumping can flow from the superconductor to the normal region in a non-dissipative way as long as the interface is gapped. When the low-energy states are present, however, as can be controlled by the Zeeman field, dissipation will occur.

Finally, while we have studied noninteracting electrons, the interplay of interactions with the weakly dispersing PLLs and superconducting correlations may lead to numerous interaction instabilities [24,56–59] and possibly to realize exotic fractional phases [22].

ACKNOWLEDGMENTS

E.S. and K.S. were supported by the US-Israel Binational Science Foundation (Grant No. 2016255). E.S. acknowledges support from ARO (W911NF-20-1-0013) and the Israel Science Foundation, Grant No. 154/19. D.S. is supported by the Israel Science Foundation, Grant No. 1790/18. M.W.B. is supported by the National Science Foundation, Grant No. DMR-2004801. The authors would like to thank R. Ilan, M. Ben Shalom, F. von Oppen, and E. Cornfeld for useful discussions.

APPENDIX A: INTERFACE DISPERSION VIA THE AKHMEROV-BEENAKKER METHOD [33]

We start with a graphene Hamiltonian containing a pseudofield, intrinsic SOC, and Zeeman terms in the valley isotropic

basis, as described in Eqs. (3), (11), and (19), and we transform it into the BdG equation in Eq. (1).

We wish to describe bound Andreev states at the SN interface, thus we follow the procedure set by [33] and start by solving Eq. (1) in the $x > 0$ normal region. The solution follows the canonical lines of PLL theory in graphene, where we adjust for the presence of SOC and Zeeman terms. We find the eigenvectors

$$\Psi(x, y) = e^{ip_y y} \begin{pmatrix} C_e^{K,\uparrow} \Phi_e^{K,\uparrow}(\xi_+) \\ C_e^{K,\downarrow} \Phi_e^{K,\downarrow}(\xi_+) \\ C_e^{K',\uparrow} \Phi_e^{K',\uparrow}(\xi_-) \\ C_e^{K',\downarrow} \Phi_e^{K',\downarrow}(\xi_-) \\ C_h^{K',\downarrow} \Phi_h^{K',\downarrow}(\xi_+) \\ C_h^{K',\uparrow} \Phi_h^{K',\uparrow}(\xi_+) \\ C_h^{K,\downarrow} \Phi_h^{K,\downarrow}(\xi_-) \\ C_h^{K,\uparrow} \Phi_h^{K,\uparrow}(\xi_-) \end{pmatrix}, \quad (\text{A1})$$

with the spinors Φ defined as

$$\Phi_e^{K,s_z}(\xi_+) = e^{-\frac{\xi_+^2}{2}} \begin{pmatrix} -i(\mu + \varepsilon + \lambda_I s_z - B_Z s_z) H_{\frac{(\mu+\varepsilon)^2 - \lambda_I^2 - 2B_Z(\mu+\varepsilon)s_z + B_Z^2}{2}}(\xi_+) \\ H_{\frac{(\mu+\varepsilon)^2 - \lambda_I^2 - 2B_Z(\mu+\varepsilon)s_z + B_Z^2}{2}}(\xi_+) \end{pmatrix}, \quad (\text{A2})$$

$$\Phi_e^{K',s_z}(\xi_-) = e^{-\frac{\xi_-^2}{2}} \begin{pmatrix} H_{\frac{(\mu+\varepsilon)^2 - \lambda_I^2 - 2B_Z(\mu+\varepsilon)s_z + B_Z^2}{2}}(\xi_-) \\ -i(\mu + \varepsilon - \lambda_I s_z - B_Z s_z) H_{\frac{(\mu+\varepsilon)^2 - \lambda_I^2 - 2B_Z(\mu+\varepsilon)s_z + B_Z^2}{2}}(\xi_-) \end{pmatrix}, \quad (\text{A3})$$

$$\Phi_h^{K',s_z}(\xi_+) = e^{-\frac{\xi_+^2}{2}} \begin{pmatrix} -i(\mu - \varepsilon - \lambda_I s_z - B_Z s_z) H_{\frac{(\mu-\varepsilon)^2 - \lambda_I^2 - 2B_Z(\mu-\varepsilon)s_z + B_Z^2}{2}}(\xi_+) \\ H_{\frac{(\mu-\varepsilon)^2 - \lambda_I^2 - 2B_Z(\mu-\varepsilon)s_z + B_Z^2}{2}}(\xi_+) \end{pmatrix}, \quad (\text{A4})$$

$$\Phi_h^{K,s_z}(\xi_-) = e^{-\frac{\xi_-^2}{2}} \begin{pmatrix} H_{\frac{(\mu-\varepsilon)^2 - \lambda_I^2 - 2B_Z(\mu-\varepsilon)s_z + B_Z^2}{2}}(\xi_-) \\ -i((\mu - \varepsilon) + \lambda_I s_z - B_Z s_z) H_{\frac{(\mu-\varepsilon)^2 - \lambda_I^2 - 2B_Z(\mu-\varepsilon)s_z + B_Z^2}{2}}(\xi_-) \end{pmatrix}, \quad (\text{A5})$$

where $s_z = \uparrow\downarrow = \pm 1$. The bound Andreev states on the interface at $x = 0$ are described using a boundary condition equation

$$(M_{NS} - 1)\Psi = 0, \quad (\text{A6})$$

where the matrix M_{NS} is given by [33,39]

$$M_{NS} = \tau_0 s_0 \left(\frac{\varepsilon}{\Delta} - i\sigma_x \sqrt{1 - \frac{\varepsilon^2}{\Delta^2}} \right). \quad (\text{A7})$$

This is similar to the BC equation presented in [33], where we include the constraint for transitions between electrons and

holes to involve opposite spins via s_0 in Eq. (A7). Solving Eq. (A6) for the wave function in Eqs. (A1)–(A5) at $x = 0$ gives the dispersion relation $\varepsilon(p_y)$. By defining

$$f_{\alpha \pm \lambda_I \mp B_Z}(p_y) \equiv \frac{H_{\frac{\alpha^2 - \lambda_I^2 \mp 2B_Z \alpha + B_Z^2}{2}}(p_y)}{(\alpha \pm \lambda_I \mp B_Z) H_{\frac{\alpha^2 - \lambda_I^2 \mp 2B_Z \alpha + B_Z^2}{2}}(p_y)}, \quad (\text{A8})$$

$$f_{\alpha \pm \lambda_I \pm B_Z}(p_y) \equiv \frac{H_{\frac{\alpha^2 - \lambda_I^2 \pm 2B_Z \alpha + B_Z^2}{2}}(p_y)}{(\alpha \pm \lambda_I \pm B_Z) H_{\frac{\alpha^2 - \lambda_I^2 \pm 2B_Z \alpha + B_Z^2}{2}}(p_y)}, \quad (\text{A9})$$

the four solutions can be written compactly as

$$f_{\mu - \varepsilon + s_z \lambda_I + s_z B_Z}(p_y) - f_{\mu + \varepsilon + s_z \lambda_I - s_z B_Z}(p_y) = \frac{\sqrt{\Delta^2 - \varepsilon^2}}{\varepsilon} [1 + f_{\mu + \varepsilon + s_z \lambda_I - s_z B_Z}(p_y) f_{\mu - \varepsilon + s_z \lambda_I + s_z B_Z}(p_y)], \quad (\text{A10})$$

$$f_{\mu - \varepsilon - s_z \lambda_I + s_z B_Z}(-p_y) - f_{\mu + \varepsilon - s_z \lambda_I - s_z B_Z}(-p_y) = \frac{\sqrt{\Delta^2 - \varepsilon^2}}{\varepsilon} [1 + f_{\mu + \varepsilon - s_z \lambda_I - s_z B_Z}(-p_y) f_{\mu - \varepsilon - s_z \lambda_I + s_z B_Z}(-p_y)]. \quad (\text{A11})$$

We solve Eqs. (A10) and (A11) for ε as a function of p_y numerically for the case in which the Zeeman field B_Z is

smaller than the first nonzero PLL to get the spectra plotted in Fig. 2.

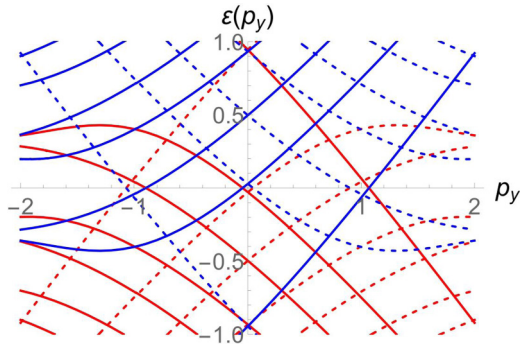


FIG. 8. Dispersion relation $\varepsilon(p_y)$ as in Fig. 2, with the parameters $\Delta = 10$, $\mu = 0$, and $B_Z = \sqrt{3}$, leading to a total of six crossings.

As B_Z increases beyond the energy of the $n \geq 1$ PLLs, more zero-energy crossings are created. To simplify the picture, we focus on $\mu = 0$, and we plot in Fig. 8 the spectrum for a value of B_Z between the first and second PLLs, $B_Z = \sqrt{3}$. When B_Z surpasses the energy of each $n > 0$ PLL, we see eight new bands that go through $E = 0$, leading to four new crossings. Two crossings appear when B_Z is equal to the energy of the LL, and another two appear when B_Z is larger.

APPENDIX B: INTERFACE DISPERSION VIA TIGHT-BINDING CALCULATIONS

To corroborate the low-energy calculations, we construct a tight-binding model of the system presented in the main text. We look at a graphene hexagonal lattice in a ribbon geometry, translationally invariant in the \hat{y} (zigzag) direction and finite in the \hat{x} (armchair) direction, where the directions are described in Fig. 1 in the main text. To create the pseudofield, we linearly change the hopping amplitude in the \hat{x} direction [22,26,60,61]. The full tight-binding Hamiltonian is

$$H_{\text{tb}} = H_G + H_Z + H_{\text{SC}}. \quad (\text{B1})$$

Here, the graphene ribbon with the pseudofield Hamiltonian reads

$$H_G = \sum_s \int \frac{dk_y}{2\pi} \left[- \sum_{\sigma} \sum_{i=1}^N \mu c_{i,\sigma,s}^\dagger(k_y) c_{i,\sigma,s}(k_y) - \sum_{i=1}^N t \cos\left(\frac{\sqrt{3}}{2} a k_y\right) c_{i,B,s}^\dagger(k_y) c_{i,A,s}(k_y) - \sum_{i=2}^N (t - \delta t(i)) (c_{i-1,B,s}^\dagger(k_y) c_{i,A,s}(k_y)) + \text{H.c.} \right], \quad (\text{B2})$$

where s runs over spin, i runs over the discretized layers of the lattice in the \hat{x} direction, t is the hopping amplitude between nearest neighbors, $\delta t(i)$ is the change in the hopping amplitude for hopping between adjacent layers, which is a function of the layer index i , and A/B is the honeycomb sublattice index. In what follows, we set $a = 1$, $t = 1$, and $dt = 0.006$. We plot the spectrum with and without a pseudofield in Fig. 9.

We add a Zeeman field

$$H_Z = \sum_{\lambda,i} \int \frac{dk_y}{2\pi} B_Z [c_{i,\lambda,\uparrow}^\dagger(k_y) c_{i,\lambda,\uparrow}(k_y) - (\uparrow \rightleftharpoons \downarrow)], \quad (\text{B3})$$

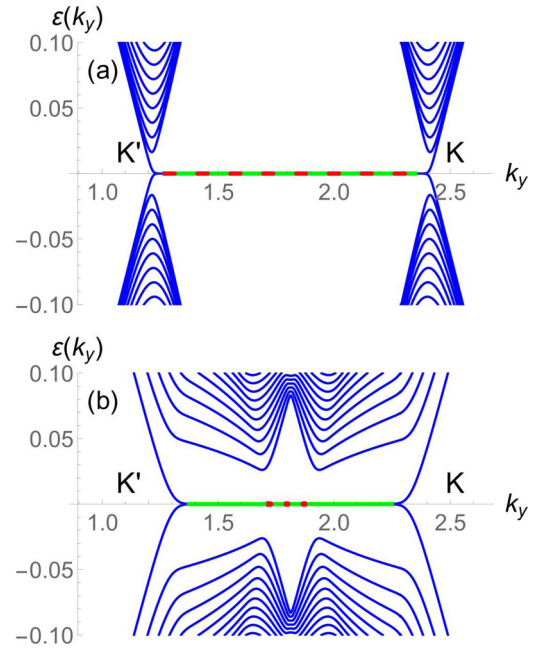


FIG. 9. Spectrum of a graphene ribbon described by the tight-binding model in Eq. (B1) without (a) and with (b) a pseudofield generated by $\delta t = 0.006$. The system size is $N_n = 140$. The green and red segments represent the zigzag edge states on the bottom and top of the ribbons, respectively, whose inversion symmetry is broken by the strain gradient in (b).

where $\lambda = A, B$ is a sublattice index and B_Z is the Zeeman amplitude. Finally, we induce superconductivity in the regions specified below, with the following Hamiltonian [26]:

$$H_{\text{SC}} = \sum_{\lambda,i \in \text{SC}} \int \frac{dk_y}{2\pi} [\Delta c_{i,\lambda,\uparrow}^\dagger(k_y) c_{i,\lambda,\downarrow}^\dagger(-k_y) + \text{h.c.} - (\uparrow \rightleftharpoons \downarrow)], \quad (\text{B4})$$

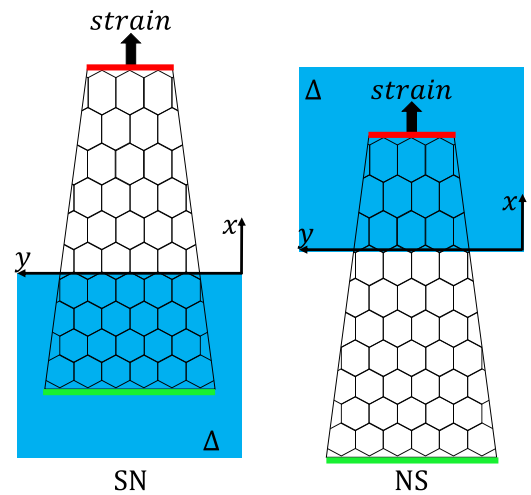


FIG. 10. Illustration of the two types of normal-superconducting interfaces we investigate in Fig. 11. In the SN configuration the superconducting region is at the bottom of the graphene ribbon, and in the NS configuration it is at the top. The zigzag edge states are color-coded in accordance with the zigzag bands in the spectra in Figs. 9 and 11.

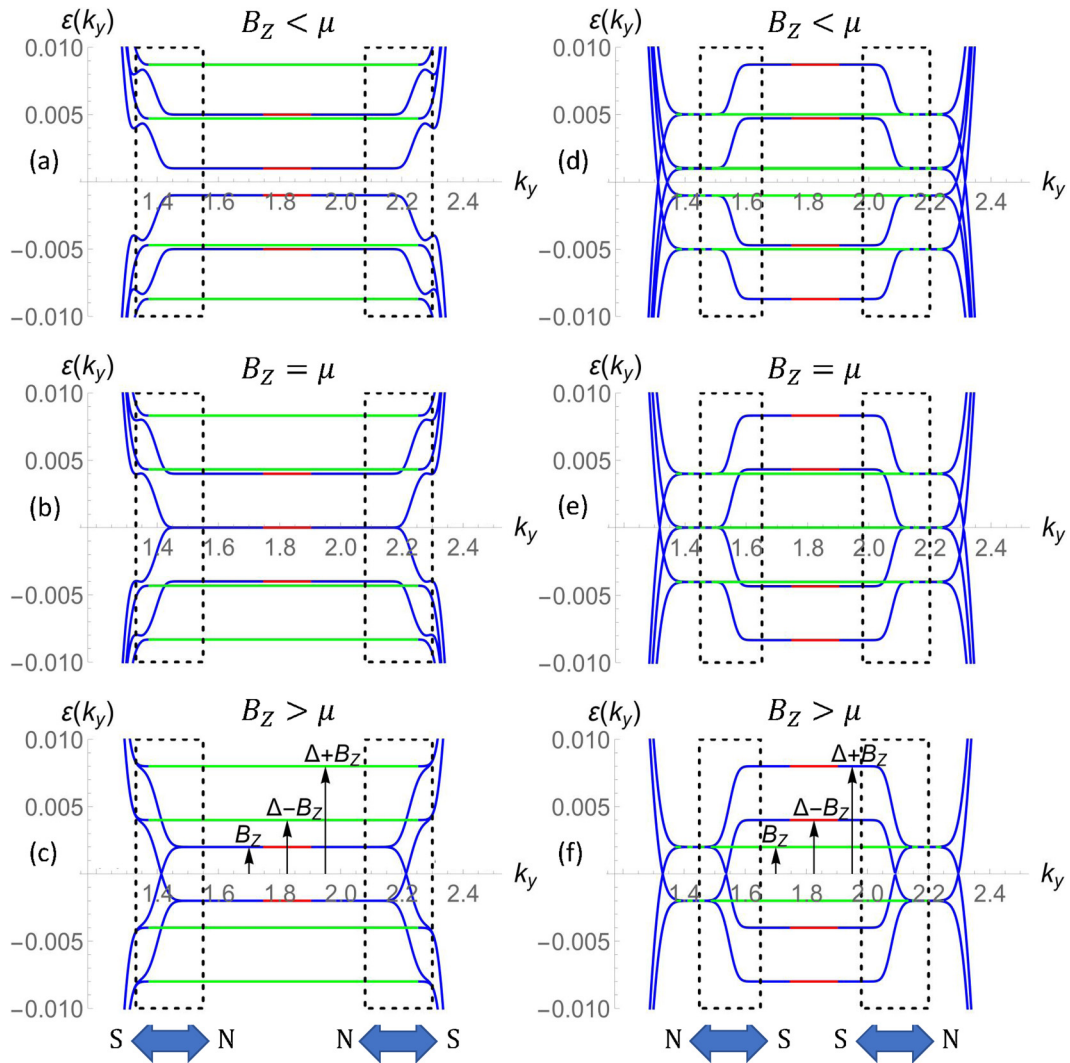


FIG. 11. Spectra of an SN [(a)–(c)] and NS [(d)–(f)] graphene ribbon interface described by the tight-binding model in Eq. (B2), with a pseudofield, a Zeeman field described by Eq. (B3), and a superconducting potential described by Eq. (B4). The size of the normal region is $N_n = 90$, the size of the superconducting region is $N_s = 50$, and we use the parameters $\delta t = 0.06$, $\Delta = 0.006$, and $B_Z = 0.002$. In (a) and (d) $\mu = 0.3$ and we see a gap on the SN interface, in (b) and (e) $\mu = 0.2$ and this gap closes, and in (c) and (f) $\mu = 0.1$ and we observe the helical states described in the main text. The dashed rectangles mark the interface between the normal and superconducting regions around each node. The green and red lines are the zigzag edge states on the bottom and top of the ribbons, respectively.

where Δ is the superconductive potential. Here $i \in \text{SC}$ refers to the sites that belong to the proximitized region.

We compute the spectrum of the tight-binding model for an interface between a normal and a superconducting region. N_s denotes the size of the superconductive region ($\Delta > 0$), and N_n denotes the size of the normal region ($\Delta = 0$). Unlike in the Akhmerov-Beenakker method and the low-energy calculations, the ribbon geometry produces zigzag edge states in the spectrum, which are different on each of the edges due to the pseudofield. We thus look at both possible configurations for the interface, i.e., one where the superconducting region is at the top edge of the ribbon (NS), and the other where the superconductive region is at the bottom edge of the ribbon (SN). Both configurations are plotted in Fig. 10. The strain gradient breaks the inversion symmetry, making these configurations nonequivalent.

We plot the spectra of the three scenarios discussed in the main text: $B_Z < \mu$, $B_Z = \mu$, and $B_Z > \mu$ for the SN and NS geometries in Fig. 11. The zigzag edge states on the bottom of the ribbon are colored green, and the zigzag edge states on the top of the ribbon are colored red. The position-momentum coupling is such that around the K node, increasing momentum corresponds to decreasing x -position, while around the K' node increasing momentum corresponds to increasing x -position. As seen in Fig. 11, specifically in panels (c) and (f) of the mentioned figures, the tight-binding calculation reproduces the helical states when $B_Z > \mu$.

1. Superconducting-vacuum interface

We now consider the zigzag graphene ribbon under (i) uniform Zeeman splitting B_Z , (ii) uniform pairing Δ , and (iii) strain gradient leading to PLLs. The resulting tight-binding

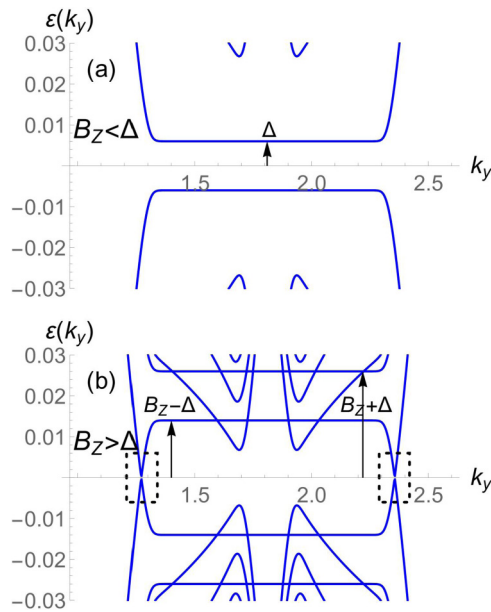


FIG. 12. Spectrum of the fully superconducting system with a pseudofield. We set $\Delta = 0.006$, $\delta t = 0.006$, and $\mu = 0$. In (a) $B_Z = 0 < \Delta$ and in (b) $B_Z = 0.008 > \Delta$. The system size is $N_s = 140$.

spectrum is shown in Fig. 12. We see that for $B_Z > \Delta$ the interface with vacuum supports gapless edge states. Therefore, our class D superconductor supports a topological nontrivial phase.

As discussed in Sec. III D, due to the S^z conservation our system maps to two models classified by the Altland-Zirnbauer class D superconductor with \mathbb{Z} index in each sector. This double-copy allows to accommodate the presence of counterpropagating modes at each interface, as seen in the small boxes in Fig. 12(b) (similar to a system of spin-up electrons under a positive orbital magnetic field and spin-down electrons under opposite field). As we discussed in depth above, the nature of each chiral mode is that of a

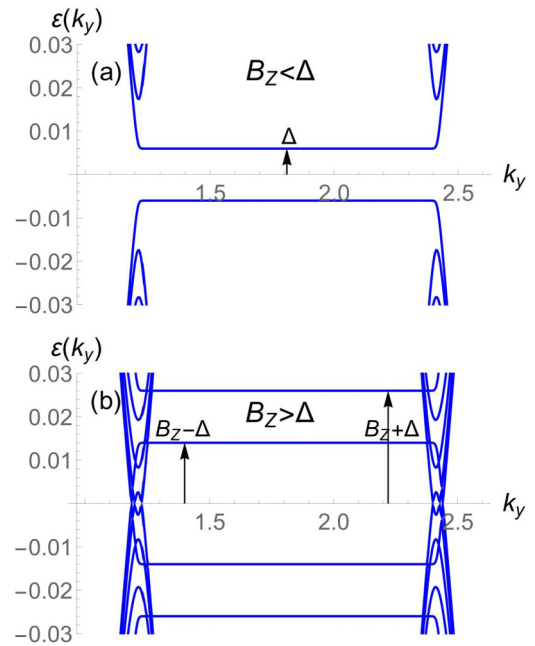


FIG. 13. Same as in Fig. 12, with $\delta t = 0$.

Dirac fermion, which can be decomposed into two Majorana fermions. Hence in each sector our topological superconductor exhibits an even \mathbb{Z} index. Presumably this can be associated with the fact that pairing connects two disconnected Fermi points in our system.

Turning off the strain, the spectrum is shown in Fig. 13. We can see that similar to the case with PLLs, the spectrum becomes gapless for $B_Z > \Delta$ even in the absence of PLLs. However, the present state is gapless in the bulk. Indeed the entire Dirac cones, which have quantized levels due to the finite stripe, cross the $\varepsilon = 0$ line. On the other hand, in the strained case of Fig. 12 the gapped modes are localized at the boundary.

- [1] N. Levy, S. Burke, K. Meaker, M. Panlasigui, A. Zettl, F. Guinea, A. C. Neto, and M. Crommie, *Science* **329**, 544 (2010).
- [2] C. Si, Z. Sun, and F. Liu, *Nanoscale* **8**, 3207 (2016).
- [3] Y. Jiang, J. Mao, J. Duan, X. Lai, K. Watanabe, T. Taniguchi, and E. Y. Andrei, *Nano Lett.* **17**, 2839 (2017).
- [4] D. Akinwande, C. J. Brennan, J. S. Bunch, P. Egberts, J. R. Felts, H. Gao, R. Huang, J.-S. Kim, T. Li, Y. Li, K. M. Liechti, N. Lu, H. S. Park, E. J. Reed, P. Wang, B. I. Yakobson, T. Zhang, Y.-W. Zhang, Y. Zhou, and Y. Zhu, *Extreme Mech. Lett.* **13**, 42 (2017).
- [5] P. Nigge, A. C. Qu, É. Lantagne-Hurtubise, E. Mårsell, S. Link, G. Tom, M. Zonno, M. Michiardi, M. Schneider, S. Zhdanovich, G. Levy, U. Starke, C. Gutiérrez, D. Bonn, S. A. Burke, M. Franz, and A. Damascelli, *Sci. Adv.* **5** (2019).
- [6] P. R. Wallace, *Phys. Rev.* **71**, 622 (1947).
- [7] K. S. Novoselov, A. K. Geim, S. V. Morozov, D. Jiang, M. I. Katsnelson, I. V. Grigorieva, S. V. Dubonos, and A. A. Firsov, *Nature (London)* **438**, 197 (2005).
- [8] Y. Zhang, Y.-W. Tan, H. L. Stormer, and P. Kim, *Nature (London)* **438**, 201 (2005).
- [9] A. H. Castro Neto, F. Guinea, N. M. R. Peres, K. S. Novoselov, and A. K. Geim, *Rev. Mod. Phys.* **81**, 109 (2009).
- [10] F. Guinea, M. I. Katsnelson, and A. K. Geim, *Nat. Phys.* **6**, 30 (2010).
- [11] M. A. Vozmediano, M. Katsnelson, and F. Guinea, *Phys. Rep.* **496**, 109 (2010).
- [12] D. I. Pikulin, A. Chen, and M. Franz, *Phys. Rev. X* **6**, 041021 (2016).
- [13] A. G. Grushin, J. W. F. Venderbos, A. Vishwanath, and R. Ilan, *Phys. Rev. X* **6**, 041046 (2016).

- [14] R. Ilan, A. G. Grushin, and D. I. Pikulin, *Nat. Rev. Phys.* **2**, 29 (2020).
- [15] E. V. Gorbar, V. A. Miransky, I. A. Shovkovy, and P. O. Sukhachov, *Phys. Rev. B* **96**, 125123 (2017).
- [16] V. Arjona and M. A. H. Vozmediano, *Phys. Rev. B* **97**, 201404(R) (2018).
- [17] S. Kamboj, P. S. Rana, A. Sirohi, A. Vasdev, M. Mandal, S. Marik, R. P. Singh, T. Das, and G. Sheet, *Phys. Rev. B* **100**, 115105 (2019).
- [18] F. Guinea, A. K. Geim, M. I. Katsnelson, and K. S. Novoselov, *Phys. Rev. B* **81**, 035408 (2010).
- [19] S. Zhu, J. A. Stroscio, and T. Li, *Phys. Rev. Lett.* **115**, 245501 (2015).
- [20] E. Sela, Y. Bloch, F. von Oppen, and M. B. Shalom, *Phys. Rev. Lett.* **124**, 026602 (2020).
- [21] L. Covaci and F. M. Peeters, *Phys. Rev. B* **84**, 241401(R) (2011).
- [22] P. Ghaemi, J. Cayssol, D. N. Sheng, and A. Vishwanath, *Phys. Rev. Lett.* **108**, 266801 (2012).
- [23] B. Uchoa and Y. Barlas, *Phys. Rev. Lett.* **111**, 046604 (2013).
- [24] B. Roy and V. Juričić, *Phys. Rev. B* **90**, 041413(R) (2014).
- [25] B. Amorim, A. Cortijo, F. de Juan, A. Grushin, F. Guinea, A. Gutiérrez-Rubio, H. Ochoa, V. Parente, R. Roldán, P. San-Jose, J. Schiefele, M. Sturla, and M. Vozmediano, *Phys. Rep.* **617**, 1 (2016).
- [26] S.-P. Lee, D. Nandi, F. Marsiglio, and J. Maciejko, *Phys. Rev. B* **95**, 174517 (2017).
- [27] G. Massarelli, G. Wachtel, J. Y. T. Wei, and A. Paramekanti, *Phys. Rev. B* **96**, 224516 (2017).
- [28] T. Liu, M. Franz, and S. Fujimoto, *Phys. Rev. B* **96**, 224518 (2017).
- [29] E. M. Nica and M. Franz, *Phys. Rev. B* **97**, 024520 (2018).
- [30] H. Khanjani and A. G. Moghaddam, *Phys. Rev. B* **98**, 195421 (2018).
- [31] A. F. Andreev, *Zh. Eksp. Teor. Fiz.* **46**, 1823 (1964) [*JETP* **19**, 1228 (1964)].
- [32] C. W. J. Beenakker, *Phys. Rev. Lett.* **97**, 067007 (2006).
- [33] A. R. Akhmerov and C. W. J. Beenakker, *Phys. Rev. Lett.* **98**, 157003 (2007).
- [34] K. G. S. H. Gunawardana and B. Uchoa, *Phys. Rev. B* **91**, 241402(R) (2015).
- [35] M. König, S. Wiedmann, C. Brüne, A. Roth, H. Buhmann, L. W. Molenkamp, X.-L. Qi, and S.-C. Zhang, *Science* **318**, 766 (2007).
- [36] D. A. Abanin, P. A. Lee, and L. S. Levitov, *Phys. Rev. Lett.* **96**, 176803 (2006).
- [37] L. Veyrat, C. Déprez, A. Coissard, X. Li, F. Gay, K. Watanabe, T. Taniguchi, Z. Han, B. A. Piot, H. Sellier, and B. Sacépé, *Science* **367**, 781 (2020).
- [38] P. San-Jose, J. L. Lado, R. Aguado, F. Guinea, and J. Fernández-Rossier, *Phys. Rev. X* **5**, 041042 (2015).
- [39] M. Titov and C. W. J. Beenakker, *Phys. Rev. B* **74**, 041401(R) (2006).
- [40] C. Xu and J. E. Moore, *Phys. Rev. B* **73**, 045322 (2006).
- [41] C. Wu, B. A. Bernevig, and S.-C. Zhang, *Phys. Rev. Lett.* **96**, 106401 (2006).
- [42] E. Sela, A. Altland, and A. Rosch, *Phys. Rev. B* **84**, 085114 (2011).
- [43] C. L. Kane and E. J. Mele, *Phys. Rev. Lett.* **95**, 226801 (2005).
- [44] C.-K. Chiu, J. C. Y. Teo, A. P. Schnyder, and S. Ryu, *Rev. Mod. Phys.* **88**, 035005 (2016).
- [45] R. Kennedy and M. R. Zirnbauer, *Commun. Math. Phys.* **342**, 909 (2016).
- [46] P. Weber, J. Güttinger, I. Tsioutsios, D. E. Chang, and A. Bachtold, *Nano Lett.* **14**, 2854 (2014).
- [47] T. Low, Y. Jiang, M. Katsnelson, and F. Guinea, *Nano Lett.* **12**, 850 (2012).
- [48] F. Amet, C. T. Ke, I. V. Borzenets, J. Wang, K. Watanabe, T. Taniguchi, R. S. Deacon, M. Yamamoto, Y. Bomze, S. Tarucha, and G. Finkelstein, *Science* **352**, 966 (2016).
- [49] M. B. Shalom, M. Zhu, V. Fal'ko, A. Mishchenko, A. Kretinin, K. Novoselov, C. Woods, K. Watanabe, T. Taniguchi, and A. Geim, *Nat. Phys.* **12**, 318 (2016).
- [50] G.-H. Lee, K.-F. Huang, D. K. Efetov, D. S. Wei, S. Hart, T. Taniguchi, K. Watanabe, A. Yacoby, and P. Kim, *Nat. Phys.* **13**, 693 (2017).
- [51] A. W. Draelos, M. T. Wei, A. Serebinski, C. T. Ke, Y. Mehta, R. Chamberlain, K. Watanabe, T. Taniguchi, M. Yamamoto, S. Tarucha, I. V. Borzenets, F. Amet, and G. Finkelstein, *J. Low Temp. Phys.* **191**, 288 (2018).
- [52] M. Zhu, M. Ben Shalom, A. Mishchenko, V. Fal'ko, K. Novoselov, and A. Geim, *Nanoscale* **10**, 3020 (2018).
- [53] G.-H. Lee and H.-J. Lee, *Rep. Prog. Phys.* **81**, 056502 (2018).
- [54] K.-F. Huang, Y. Ronen, R. Mélin, D. Feinberg, K. Watanabe, T. Taniguchi, and P. Kim, *arXiv:2008.03419*.
- [55] O. Gül, Y. Ronen, S. Y. Lee, H. Shapourian, J. Zauberman, Y. H. Lee, K. Watanabe, T. Taniguchi, A. Vishwanath, A. Yacoby, and P. Kim, *arXiv:2009.07836*.
- [56] I. F. Herbut, *Phys. Rev. B* **78**, 205433 (2008).
- [57] V. J. Kauppila, F. Aikebaier, and T. T. Heikkilä, *Phys. Rev. B* **93**, 214505 (2016).
- [58] F. Xu, P.-H. Chou, C.-H. Chung, T.-K. Lee, and C.-Y. Mou, *Phys. Rev. B* **98**, 205103 (2018).
- [59] T. J. Peltonen and T. T. Heikkilä, *J. Phys.: Condens. Matter* **32**, 365603 (2020).
- [60] W.-Y. He and L. He, *Phys. Rev. B* **88**, 085411 (2013).
- [61] É. Lantagne-Hurtubise, X.-X. Zhang, and M. Franz, *Phys. Rev. B* **101**, 085423 (2020).